Nuclear quadrupole resonance single-pulse echoes

David W. Prescott [a,*], Joel B. Miller [b], Chris Tourigny [a], Karen L. Sauer [a]

[a] Department of Physics and Astronomy, George Mason University, 4400 University Drive MS 3F3, Fairfax, VA 22030, USA
[b] Naval Research Laboratory Code 6122 Washington, DC 20375-5342, USA

ARTICLE INFO

ABSTRACT

We report the first detection of a spin echo after excitation of a powder sample by a single pulse at the resonance frequency during nuclear quadrupole resonance (NQR). These echoes can occur in samples that have an inhomogeneously broadened line, in this case due to the distribution of electric field gradients. The echoes are easily detectable when the Rabi frequency approaches the linewidth and the average effective tipping angle is close to 270°. When limited by a weak radio-frequency field, the single-pulse echo can be used to increase the signal to noise ratio over conventional techniques. These effects can be used to optimize the NQR detection of contraband containing quadrupole nuclei and they are demonstrated with glycine hemihydrochloride and hexhydro-1,3,5-trinitro-1,3,5-triazine (RDX).

1. Introduction

The use of NQR for the detection of contraband material has received significant attention because of its ease of implementation and ability to uniquely identify illicit substances [1–4]. Practical considerations push NQR detection technology to operate at lower magnetic fields for reduced power requirements, larger detection volumes, and safe operation around delicate instrumentation. Therefore, to improve the NQR detection capability it is important to understand the spin-dynamics which occurs in samples irradiated by weak radio-frequency (rf) pulses. One clear manifestation of the spin-dynamics in this regime is the appearance of an echo after a single pulse, of duration t_1, in samples that have a distribution of electric field gradients (EFG's) which result in an inhomogeneously broadened line, which we will refer to as EIB – Electric field gradient Inhomogeneously Broadened. In Fig. 1 the echo effect on the experimental signal (○) can clearly be seen as compared to delta function pulses (solid line). While these data are for $\gamma B_1/\sigma = 2.6$, where γ is the gyromagnetic ratio, B_1 is the amplitude of the applied rf, and σ is the linewidth (half-width at half maximum) of the sample, we will demonstrate that more pronounced single-pulse echoes (SPEs) occur when $\gamma B_1/\sigma$ is even lower. Theoretically we explore the signal size, timing, and optimal pulse duration to observe these SPEs and compare them to the traditional echo from a double pulse in this low field regime.

The first observation of single-pulse echoes was by Bloom [5] in 1954 using water in a very inhomogeneous magnetic field. Since then, they have been detected in a number of other physical sys-

tems, such as: magnetically ordered solids [6–10], crystals with large dynamic frequency shifts [11], or an optically thin molecular sample subjected to a Stark-pulse [12]. It has long been debated the exact method of formation of these observed echoes [7,13–15], and under what conditions they are formed—whether for large inhomogeneous broadening alone [5], or with the addition of significant inhomogeneity in the Rabi frequencies [7], or for rf excitation far detuned from the center frequency [16–18]. These echoes, however, share in common the experimental observation of the signal's peak at times comparable to the duration of the excitation pulse, typically after a tipping pulse $\geqslant 360°$. In contrast, we report on a SPE which occurs for an average effective tipping angle close to 270°, and whose signal peaks much closer to the falling edge of the pulse. This SPE, which is closely related to the more traditional double-pulse echo (DPE) [19], can be most easily observed under conditions of inhomogeneous line broadening and inhomogeneous Rabi frequencies, which in the case of NQR corresponds to a large EIB and a distribution of crystallite directions as found in a powder sample. Fig. 1 demonstrates the increase in signal because of this echo effect under these conditions.

2. Theory

To demonstrate the formation of NQR SPEs we subject a system dominated by the nuclear quadrupole interaction to a single resonant rf pulse, include offset resonance effects due to the linewidth, and model the response. Additionally, we assume that relaxation is negligible during the pulse and that the wait time between data acquisitions is much greater than both the spin-lattice relaxation time (T_1) and the spin-spin relaxation time (T_2) (in contrast to multipulse SPEs [20]). This admittedly simplified model is suffi-
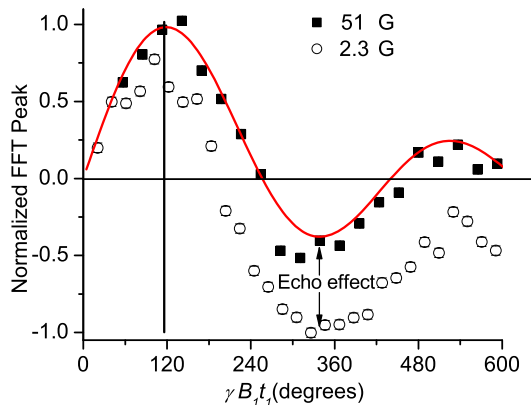
Fig. 1. By comparing the signal from RDX due to a delta-like pulse to the signal from a weaker pulse the formation of a NQR SPE is demonstrated. The normalized NQR signal in Fourier space vs. tipping angle for a single pulse of $B_1 = 51$ G closely follows the predicted NQR signal [21] (solid line) while the ($\bigcirc$) shows the signal for a pulse of 2.3 G, which produces an echo. The arrows highlight the occurrence of the maximum echo. The vertical line, at 119°, shows the point of maximum expected FID due to a delta-like pulse.

cient to show how the NQR SPE forms and to predict the conditions for a maximum echo. We deem a SPE as the occurrence of a single maximum of the signal magnitude which occurs after the end of the rf pulse. Those signals where the maximum occurs at the end of the rf pulse are deemed to be a "free decay."

The development of the SPE is modeled by the density matrix $\rho(t)$ for the total Hamiltonian $H_T = H_0 + H_1$, where H_0 is the dominant Hamiltonian and H_1 is the perturbation Hamiltonian. The dominant Hamiltonian is proportional to the quadrupole Hamiltonian and for ease of calculation the quadrupole Hamiltonian, for spin-1, can be defined with respect to fictitious spin-$\frac{1}{2}$ operators [21–23] as,

$$H_Q = \hbar \left\{ \omega_x I_{x3} + \frac{1}{3}(\omega_y - \omega_z)I_{x4} \right\}, \tag{1}$$

where $\langle I_{x3} \rangle = \frac{N_+ - N_0}{2N}$ (half the difference in population of the highest eigenstate N_+, and the lowest eigenstate N_0, over the total number of spin-1 atoms N). The definition of the three characteristic transi-

tion frequencies ($|\omega_x| > |\omega_y| > |\omega_z|$) and the operator I_{x4} (which does not contribute to the signal) can be found in the Appendix. The fictitious spin-$\frac{1}{2}$ formalism allows us to treat a multi-level system as a two level system when only one transition is involved, for instance ω_x. While we focus on the case of spin-1, because of our application, our results are generally applicable to any non-degenerate two level system coupled by an rf field, i.e. either a spin-$\frac{1}{2}$ or a fictitious spin-$\frac{1}{2}$ system [24].

We treat as a perturbation the interaction of the nuclei with the rf pulse of frequency ω_{rf} and the off-resonant part of the quadrupole Hamiltonian. Therefore, the dominant Hamiltonian is written as, $H_0 \equiv \frac{\omega_{rf}}{\omega_x} H_Q$, and the perturbing Hamiltonian as, $H_1 = H_{rf} + V$, where $V \equiv -\frac{\Delta\omega}{\omega_x} H_Q$ and $\Delta\omega \equiv \omega_{rf} - \omega_x$ describe the resonance offset effects created by the EIB [25]. The rf Hamiltonian for the ω_x transition is $H_{rf} = -\gamma\hbar\mathbf{I} \cdot \mathbf{B}_1 \cos(\omega_{rf}t + \phi_1)$ where ω_{rf} is applied at $\bar{\omega}_x$, the mean value of ω_x or the first moment of the lineshape [26]. The rotation angle of the pulse is $\theta = \gamma B_1 t_1$. Note, this model is limited to systems such that the frequency difference between the NQR levels is much greater than the linewidth of the transition.

Thus, the density matrix $\rho(t)$ evolves under the Liouville equation, $\dot{\rho}\hbar = i[\rho, H_0 + H_1]$, which in the interaction representation of H_0 becomes, $\dot{\tilde{\rho}}\hbar = i[\tilde{\rho}, \widetilde{H}_1]$, where $\tilde{\rho} = e^{iH_0t/\hbar}\rho e^{-iH_0t/\hbar}$ and $\widetilde{H}_1 = \widetilde{H}_{rf} + \widetilde{V} = e^{iH_0t/\hbar}(H_{rf} + V)e^{-iH_0t/\hbar}$. Using the secular approximation [23],

$$\widetilde{H}_{rf} = -\hbar\omega_1(I_{x1}\cos\phi_1 + I_{x2}\sin\phi_1), \tag{2}$$

where the effective Rabi frequency, $\omega_1 = \gamma B_1 \cos\xi$, and ξ is the angle between the direction of the applied field and $\hat{x}$ of the principle axes frame of the EFG [26]. We then calculate $\tilde{\rho}$ in the fictitious spin-$\frac{1}{2}$ space.

In this space there is a coordinate frame for each NQR frequency [4,21]. For the ω_x NQR frequency we describe $\tilde{\rho}$ in the $\widehat{I}_{x1}, \widehat{I}_{x2}, \widehat{I}_{x3}$ subspace. Fig. 2 shows the rotation of $\tilde{\rho}$ during an rf pulse for different resonance offsets in a single crystal. After a pulse of t_1,

$$\tilde{\rho}(t_1) = e^{-i\widetilde{H}_1 t_1/\hbar}\rho(0)e^{i\widetilde{H}_1 t_1/\hbar}, \tag{3}$$

where $\widetilde{H}_1 = -\omega_t\hbar\hat{n}$ creates nutation at a rate of $\omega_t = \sqrt{\Delta\omega^2 + \omega_1^2}$ around the axis $\hat{n} = \cos\alpha\cos\phi_1\widehat{I}_{x1} + \cos\alpha\sin\phi_1\widehat{I}_{x2} + \sin\alpha\widehat{I}_{x3}$. Starting from thermal equilibrium and in the high temperature limit, $\rho(0) = -\hbar\bar{\omega}_x I_{x3}/(3kT)$, where we have neglected terms which do
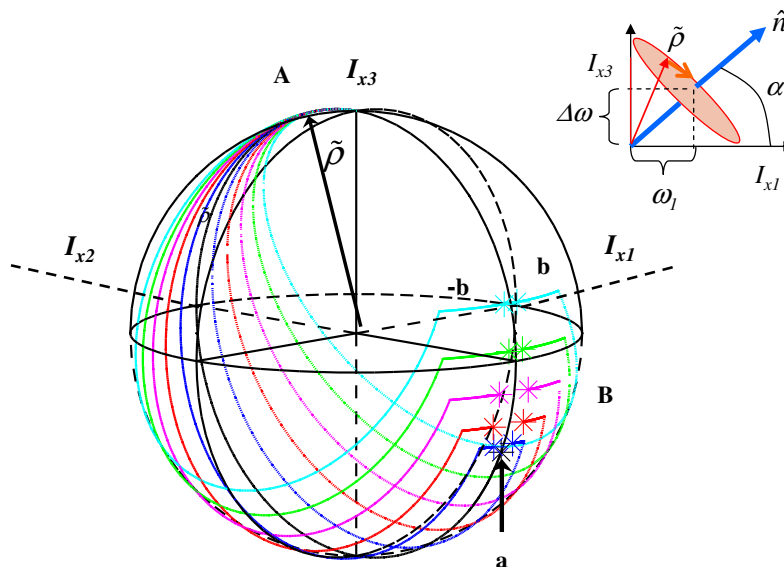

Fig. 2. The rotation of $\tilde{\rho}$ by the effective rf excitation in the presence of resonance offset effects shows the formation of the SPE. The spin isochromats start at (A), are subjected to a 270° pulse with $\phi = 0$, and then evolve till they rephase at (B) where an echo is formed. The on-resonance spin is labeled a and the amount of resonance offset for each spin progresses to the two spins subjected to the most resonance offset labeled $\pm b$, which has a $\Delta\omega$ of $\pm 2\sigma$.

not contribute to the final signal. The deviation of the rotation axis from the $\hat{I}_{x1} - \hat{I}_{x2}$ plane is, $\alpha = \arctan\frac{\Delta\omega}{\omega_1}$, as shown in inset of Fig. 2. After the rf pulse, the different spin isochromats rephase to form an echo, as shown by the horizontal lines on the surface of the sphere. This reversal of spins creates the NQR SPEs that are observed. Therefore the resonance offset, acting as an additional rotation in the $\hat{I}_{x3}$ direction, serves both to separate the isochromats during the pulse and refocuses them afterwards. The actual refocusing occurs over an extent of time, creating an echo which is smeared out temporally. A similar echo effect occurs for a powder sample, but the $\hat{I}_{x1}$ component of the rotation varies depending on the orientation of the crystallite with respect to the applied radio-frequency. The $\hat{I}_{x3}$ component of rotation, however does not vary depending on the crystallite orientation; therefore there is less variation in the nutation rate, ω_t, than when there is no off-resonance component in the rotation. For a powder, this means that the EFG inhomogeneities compensates for the Rabi inhomogeneities in a weak-field limit for a rotation of approximately 340°

Proceeding from Eq. (3), we find at a time τ_1 after the pulse,

$$\tilde{\rho}(t_1 + \tau_1) = -\frac{\hbar\bar{\omega}_x}{3kT}\left\{\frac{I_{x3}}{2}(\cos^2\alpha\cos\Theta_1 + \sin^2\alpha) - (iI_+ D_1 e^{i\delta_1}e^{i(\Delta\omega\tau_1 - \phi_1)})\right\} + \text{h.c.}, \quad (4)$$

where $\Theta_1 = \omega_t t_1$, $D_1 = \cos\alpha(\sin^2\Theta_1 + (1 - \cos\Theta_1)^2\sin^2\alpha)^{1/2}$, $\delta_1 = \arctan\frac{(1 - \cos\Theta_1)\sin\alpha}{\sin\Theta_1}$, and h.c. stands for the Hermitian conjugate. Note that Θ refers to the effective rotation each spin is subject to while θ refers to the rotation angle of the rf pulse that is applied during a pulse sequence.

The observable of interest is $\langle I_x\rangle_{SPE} = \text{Tr}(\rho I_x)$ and using the expressions for fictitious spin-$\frac{1}{2}$, we determine that,

$$\langle I_x\rangle_{SPE} = \frac{i\hbar\bar{\omega}_x e^{-i\bar{\omega}_x t}}{6kT} e^{i(\Delta\omega\tau_1 - \phi_1)}D_1 e^{i\delta_1} + \text{c.c.}, \quad (5)$$

where c.c. is the complex conjugate of the first term. This expression is similar to those seen for magnetization in spin-$\frac{1}{2}$ systems subject to Larmor inhomogeneous broadening [16].

To gain insight into the appearance of the SPE, we look in the limit when $\gamma B_1 \gg \Delta\omega$. To first order in $\frac{\Delta\omega}{\gamma B_1}$

$$\delta_1 \approx \frac{\tan(\gamma B_1 t_1 \cos\xi/2)}{\gamma B_1 \cos\xi}\Delta\omega, \quad (6)$$

and

$$D_1 \approx \sin(\gamma B_1 t_1 \cos\xi), \quad (7)$$

where δ_1 is the phase and D_1 is the echo amplitude. An echo-like behavior will occur when the coefficient in front of $\Delta\omega$ in Eq. (6) is negative, i.e., $180° < \gamma B_1 t_1 \cos\xi < 360°$. The amplitude, D_1, is maximum in this range when $\gamma B_1 t_1 \cos\xi$ is 270°. Under this condition, the echo would occur at $\tau_1 = \frac{1}{\gamma B_1 \cos\xi}$, which clearly demonstrates the smaller the excitation field, B_1, the increased time, after the pulse, before the occurrence of the echo.

We observe a signal from the rf pick-up coil with its axis of symmetry along the $\hat{x}$-axis. For a powder we must average over all possible directions to get,

$$\text{Signal}_{powder} = \frac{1}{2}\int\int\langle I_x\rangle_{SPE}$$
$$f(\Delta\omega)\cos\xi\sin\xi\,\mathrm{d}\xi\,\mathrm{d}\Delta\omega, \quad (8)$$

where $f(\Delta\omega)$ gives the shape of the resonance line. Experimentally we observe Lorentzian line shapes, therefore in the foregoing we assume $f(\Delta\omega)$ has a Lorentzian distribution.

To compare the SPE to the DPE, we look at the spin dynamics after a second pulse of the same strength and frequency and determine

$$\langle I_x\rangle = \frac{i\hbar\bar{\omega}_x}{6kT}e^{-i\bar{\omega}_x t}\{e^{i(\Delta\omega\tau_2 + \delta_2 - \phi_2)}D_2(\cos^2\alpha\cos\Theta_1 + \sin^2\alpha)$$
$$+ \frac{D_1}{2}[e^{i(\Delta\omega(\tau_1 + \tau_2) + \delta_1 - \phi_1)}\{\cos^2\alpha + \cos\Theta_2(1 + \sin^2\alpha)$$
$$+ 2i\sin\Theta_2\sin\alpha\} - e^{i(\Delta\omega(\tau_2 - \tau_1) - \delta_1 - (2\phi_2 - \phi_1))}$$
$$\{\cos^2\alpha + \cos\Theta_2(\sin^2\alpha - 1)\}]\} + \text{c.c.}, \quad (9)$$

where Θ_2, δ_2, and D_2 are defined with respect to the second pulse of width t_2 and phase ϕ_2.

The first term in Eq. (9) corresponds to a free induction decay (FID) from the second pulse, the second term to the FID from the first pulse, and the third term to the DPE, $\langle I_x\rangle_{DPE}$. One can easily see the third term is the DPE from the fact that the phase goes to zero at $\tau_2 = \tau_1$ in the presence of any resonance offset and in the limit of delta-function pulses. The echo signal for a powder after a double-pulse "Exorcycle" [27] sequence, that is phase cycled to leave only the echo, is then calculated from $\langle I_x\rangle_{DPE}$.

Additionally, the inclusion of the resonance offset effects in Eq. (9), predicts the delay ($\Delta\tau$) of the DPE. This delay is defined as the difference between the occurrence of the peak of the DPE due to a weak-pulse with resonance offset effects, compared to the occurrence of the peak of the DPE due to a delta-pulse. Equivalently, $\Delta\tau = t_{echo} - \tau_1$, where t_{echo} is the time of the maximum echo as shown in Fig. 3. The model predicts that the delay in the appearance of the maximum DPE approaches $\Delta\tau = 0.62t_1$ at large values of $\gamma B_1/\sigma$ in a powder and is only 2% less at small values of $\gamma B_1/\sigma$. This increased delay compares well to the prediction by Slichter [26] of $\Delta\tau = 2t_1/\pi$ in the case of protons in a static magnetic field irradiated by a perpendicular rf.

Using our model, the SPE, DPE and FID characteristics of a powder and a crystal are plotted in Fig. 4. For each value of $\gamma B_1/\sigma$ we optimize the rotation angle(s) (θ_1 and/or θ_2) to produce the maximum Signal$_{total}$, where Signal$_{total}$ is the total integrated magnitude of the signal over time and is equivalent to the amplitude in Fourier space at $\bar{\omega}_x$. In pane (a) the maximum σSignal$_{total}$ is plotted because it highlights the behavior independent of the line width with constant line shape. The sequence used to generate the DPE has no time between pulses and is phase cycled to leave only the echo. Both the SPE and DPE signals are normalized to the maximum FID due to a delta-pulse with the optimum rotation angle. The time of occurrence of the peak, after the last pulse, is shown in (d) in units of σt_{echo} radians.

Inspecting the graphs, as $\gamma B_1/\sigma$ increases, pane (d) shows that for both a powder and a crystal the maximum SPE occurs near the end of the pulse and nothing distinguishes it from a "free decay." Additionally, as $\gamma B_1/\sigma$ increases, the other characteristics approach the values predicted by delta-pulse theory. For instance, for the crystal, at large $\gamma B_1/\sigma$, the FID, SPE, and DPE Signal$_{total}$ approaches 1, while the powder DPE signal approaches 0.83. Also, at large $\gamma B_1/\sigma$, the DPE rotation angles for a powder approach $\theta_1 = 119°$ and $\theta_2 = 238°$ vs. $\theta_1 = 90°$ and $\theta_2 = 180°$ for a crystal. In particular, for large values of $\gamma B_1/\sigma$, notice that for a crystal the DPE and SPE σSignal$_{total}$ are similar but for a powder the DPE and SPE σSignal$_{total}$ differ significantly.

Contrast this with the σSignal$_{total}$ at small values of $\gamma B_1/\sigma$: for both a powder and a crystal, the DPE and SPE σSignal$_{total}$ are not
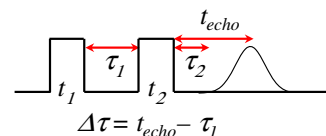

Fig. 3. SPE and DPE sequence timing diagram. Note, τ_2 is the time after the second pulse and that $t = t_1 + \tau_1 + t_2 + \tau_2$ is the total time.
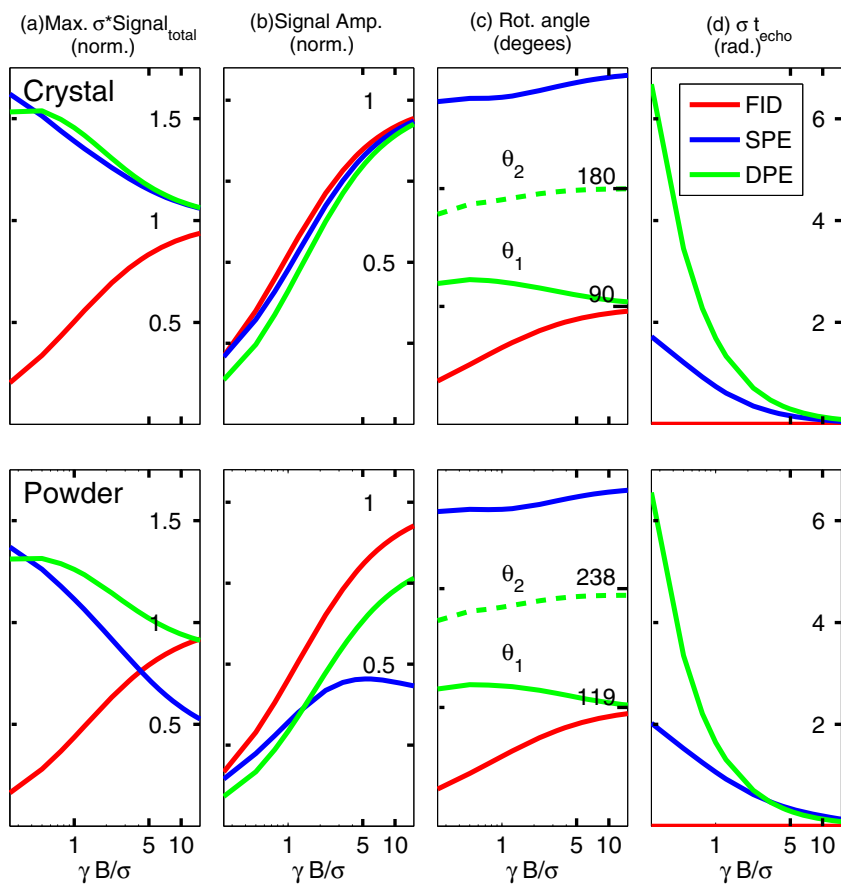
Fig. 4. NQR FID, SPE, and DPE characteristics are shown as a function of $\gamma B_1/\sigma$ for both a powder (bottom four panes) and a crystal (top four panes): (a) shows the normalized maximum total signal for each pulse in dimensionless units of $\sigma Signal_{total}$, (b) shows the normalized maximum signal amplitude in time, (c) shows the rotation angles for the maximum in (a), and (d) shows the time of occurrence of the maximum in (b).

significantly different. In fact, for a powder, as $\gamma B_1/\sigma$ decreases, the SPE $\sigma Signal_{total}$ approaches the DPE $\sigma Signal_{total}$ and exceeds it. This implies that the SPE behaves like the DPE, with no time between pulses and when it is phase cycled to leave only the echo. Also notice that the maximum amplitude of the signal is reduced, but the $\sigma Signal_{total}$ is not. This means the signal will be stretched out in time, which we observe in the experimental data. Further, in this regime, both the optimum rotation angles and the corresponding $\sigma Signal_{total}$ for a FID signal are decreasing as the dephasing during the pulse starts to dominate the spin dynamics. In comparison, the peak of the SPE occurs further from the end of the pulse, for small values of $\gamma B/\sigma$, allowing for more of the signal to be observed.

The largest variation in the SPE $\sigma Signal_{total}$ occurs in a powder between the $\sigma Signal_{total}$ after an ideal delta-function pulse and the $\sigma Signal_{total}$ after a weak rf producing a small $\gamma B_1/\sigma$ ratio. Thus, increased Rabi inhomogeneous broadening contributes to the detection of these SPEs. Therefore, we can predict from our model, that the SPE will be most noticeable in a powder with small $\gamma B_1/\sigma$ ratios. A small $\gamma B_1/\sigma$ results when the rf pulse is weak and/or the resonance has a large linewidth. Additionally, in this regime the SPE $\sigma Signal_{total}$ is comparable to and can be somewhat greater than the DPE $\sigma Signal_{total}$, as confirmed experimentally in Fig. 5.

3. Experimental conditions

The NQR SPE and DPE experiments were conducted at room temperature with two powder samples that contain ^{14}N nuclei: 17g of RDX ($C_3H_6N_6O_6$) at the NQR frequency $|\nu_y| = 3.36$ MHz with a linewidth, full-width at half-max (FWHM), of 524 ± 25 Hz, and
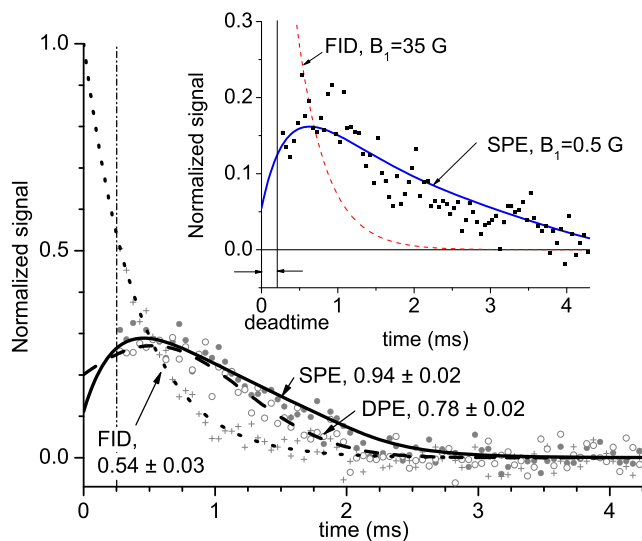

Fig. 5. In the inset, the emergence of the SPE is demonstrated using glycine hemihydrochloride. The echo (solid line) is shown in comparison to the FID from a delta-like pulse (dashed line). In the main graph is a comparison of the SPE, DPE and the optimum FID signal showing the experimental $Signal_{total}$ for each pulse sequence excluding deadtime. The SPE (solid line) due to pulses of $B_1 = 1.3$ G is compared to the DPE (dashed line) due to pulses of $B_1 = 1.3$ G and the optimum FID (dotted line) of $B_1 = 35$ G. Under these conditions the SPE $Signal_{total}$ is larger than the DPE and the FID $Signal_{total}$. The deadtime in the main graph is 0.25 ms and is 0.2 ms in the inset.

40 g of glycine hemihydrochloride ($C_4H_{10}N_2O_4$ HCL) at the v_x frequency of 0.834 MHz with a linewidth of 780 ± 30 Hz. Both samples have a predominantly Lorentzian shaped linewidth profile.

The experiments were conducted using a TecMag NQR spectrometer and a different probe for each sample. The probe consisted of the sample at the center of the tuned rf coil which was inside a Faraday cage to minimize rf interference. The probe for the glycine hemihydrochloride experiments had a Q of 30 while the probe for RDX experiments had a Q of 150.

4. Experimental results

The theory developed in the previous section allows us to select samples and design experiments to demonstrate and explore these NQR SPEs. The theory indicates the SPEs will be easier to detect as $\gamma B_1/\sigma$ is reduced since the echo signal will be temporally removed from the experimental deadtime. Using a reduced $\gamma B_1/\sigma$ of 0.43, the appearance and development of the SPE is demonstrated in the inset of Fig. 5. The SPE is produced with a pulse of $t_1 = 5$ ms, $B_1 = 0.54$ G, and $\theta_1 = 300°$: θ_1 is selected to generate the maximum SPE by referring to Fig. 4(c). The delta-like pulse (strong-pulse) is $t_1 = 31$ μs, $B_1 = 35$ G, and $\theta_1 = 119°$. The SPE clearly appears with fast initial rise and an asymmetrical tail.

T_2 effects also impact the echo signal. The theoretical echo data in the inset of Fig. 5 is adjusted down by 20% to fit the experimental echo signal profile. The adjustment reflects T_2 effects *during* the pulse.

A further demonstration of the SPE is shown in Fig. 6 as the pulse length is increased. The lower graph shows the experimental (dots) and the theoretical (line, Eq. (8)) normalized SPE signal as θ is varied for the same pulse length as in the top graph. In the top graphs of Fig. 6 the most negative values indicated the time of occurrence of the maximum theoretical SPE for a particular θ. In (a) and (d) a strong delta-like rf pulse does not show an echo while in (c) and (f) the black region shows the emergence of the SPE echo with a much weaker rf pulse. Notice that as t_1 is increased the FID maximum amplitude decreases and the SPE maximum amplitude increases. In (c) and (f) a pulse of $t_1 = 2.4$ ms is used to irradiate glycine hemihydrochloride, which has a larger linewidth than RDX, and the echo reaches a maximum where predicted ($\theta = 340°$) and is more noticeable.

Additionally, under certain conditions, the SPE $\sigma Signal_{total}$ is greater than the DPE $\sigma Signal_{total}$. In Fig. 5, a comparison of the SPE and DPE and the optimum FID $\sigma Signal_{total}$ using glycine hemihydrochloride is shown. The SPE and DPE were generated with rf pulses to create the same $\gamma B_1/\sigma$ ratio. The SPE signal, created with $B_1 = 1.3$ G, $t_1 = 2.4$ ms and $\theta_1 = 345°$ (solid line), is compared to the DPE signal, created with pulses of $B_1 = 1.3$ G, $\theta_1 = 116°$ and $\theta_2 = 187°$ (dashed line). The optimum FID is also presented (dotted line - same pulse parameters as in the inset). The experimental $\sigma Signal_{total}$, excluding deadtime, and normalized to the optimum FID, is shown for each pulse. The SPE $\sigma Signal_{total}$ (0.94 ± 0.02) is greater than the DPE $\sigma Signal_{total}$ (0.78 ± 0.02). Theoretically the SPE $\sigma Signal_{total}$ is predicted to be 0.96 while the DPE $\sigma Signal_{total}$ is 0.98. One possible cause of this difference between predicted and actual DPE $\sigma Signal_{total}$ is the breaking of the spin-locking [28] by using phase cycling in the DPE sequence. The phase cycling removes all but the DPE from the signal, but at the cost of breaking the spin-locking, hence, the signal would be lower than predicted. If a lower $\gamma B_1/\sigma$ ratio is used the calculations (Fig. 4a) for a powder show that the SPE will be greater than the DPE $\sigma Signal_{total}$, even without this spin-locking effect.

In comparison to the FID both the SPE and DPE $\sigma Signal_{total}$ are approximately twice the FID $\sigma Signal_{total}$, if the deadtime is taken
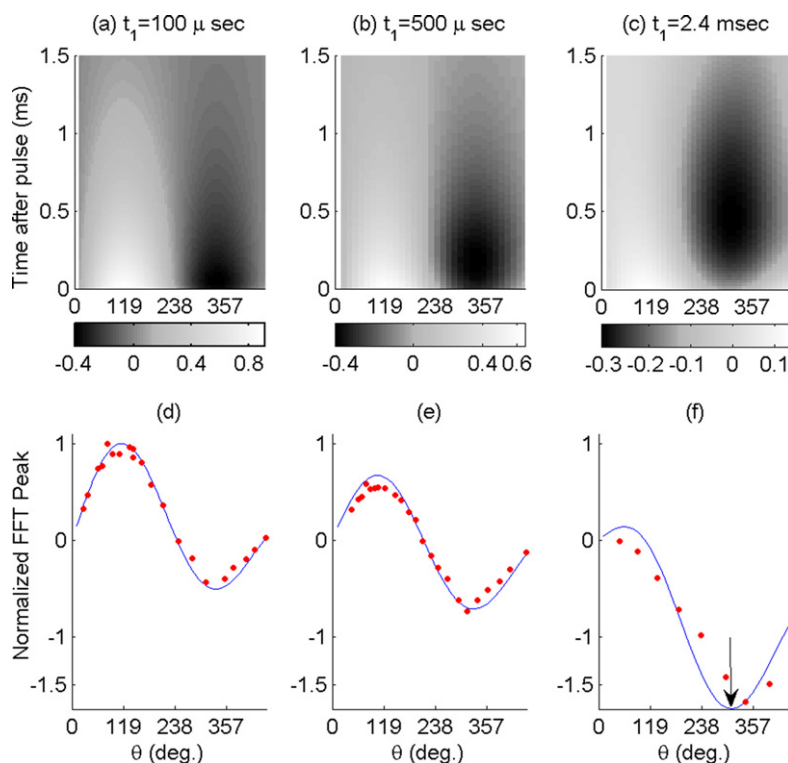

Fig. 6. Development of an SPE as the pulse length is increased. The top graphs are contour plots of the normalized theoretical SPE signal for specific θ's (x-axis) as the echo evolves in time (y-axis). The bottom graphs show the signal vs. θ for the same pulse length as the top graph. In (a) and (d) there is no observable echo after a pulse of $t_1 = 100$ μs, using RDX, while in (c) and (f) there is a noticeable echo—the black region in (c). In (b) and (e), again using RDX, the echo starts to form about 0.25 ms after a pulse of $t_1 = 500$ μs at $\theta = 345°$. In (c) and (f), using glycine hemihydrochloride, the echo is maximum about 0.5ms after a pulse of $t_1 = 2.4$ ms. Arrow in (f) points out maximum echo.
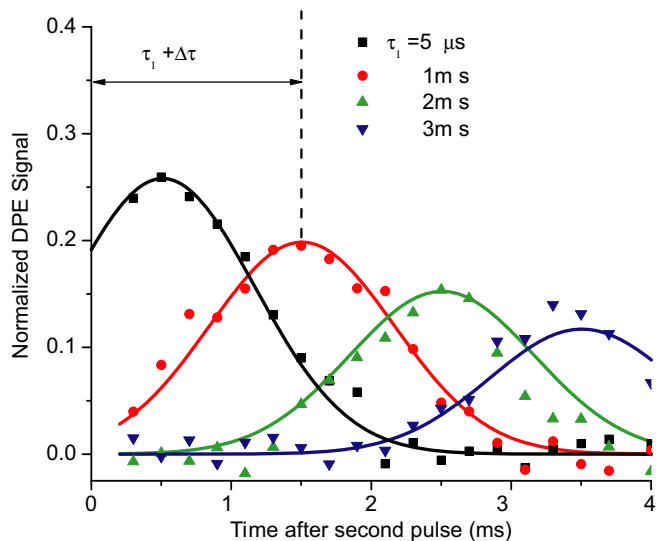
Fig. 7. Consistent delay ($\Delta\tau$) of the DPE is confirmed with weak rf pulses. Glycine hemihydrochloride is irradiated with an rf field such that $\gamma B_1/\sigma = 1.03$. Four normalized DPEs, with different values of τ_1, are plotted vs. time after the second pulse. The fits (solid lines) show a constant delay of $\Delta\tau = 0.56$ ms.

into account, which shows the potential increase in attainable signal when using these pulse sequences in comparison to the FID. The FID from the strong-pulse has a sharply decreasing amplitude and may be difficult to detect experimentally due to the implementation dependent deadtime. In contrast, the occurrence of the SPE is significantly removed from the trailing edge of the pulse so it is easier to detect experimentally.

In Fig. 7, the delay ($\Delta\tau$), predicted by our model, of the occurrence of the DPE is demonstrated. The delay is the difference between our theoretical predictions and the predictions using an ideal delta-pulse. The pulse to generate the DPE is $B_1 = 1.3$ G, $\theta_1 = 116°$, and $\theta_2 = 187°$, while θ_1 and θ_2 are optimized for maximum DPE signal by referring to Fig. 4(c). Data shows the peak normalized signal decreasing with increasing τ_1, while there is a consistent delay in the formation of the echo. In Fig. 7, the echo signal is shown and each data point is the average of 200 μs of data. The raw echo time data are then fit to a Gaussian (solid lines) because it has been shaped by the pulse and our numerical simulations predict that it is roughly Gaussian under these conditions. The fit of the four data sets result in a $T_2 = 7.6 \pm 0.1$ ms, with a Gaussian standard deviation of 1.32 ± 0.01 ms, in comparison to a predicted value of 1.53 ms, and a consistent delay of $\Delta\tau = 0.56 \pm 0.01$ ms in comparison to 0.51 ms. The predictions are generated using Eq. (9) and the differences could be due to non-ideal pulses, and relaxation effects.

5. Conclusion

NQR SPEs have been detected for the first time and are well modeled by a theory that incorporates EFG inhomogeneous broadening. The theory demonstrates that the echoes are created by the dephasing and rephasing of the individual spin isochromats that are present in a material with a large EIB. The SPEs occur in a powder when θ is $\approx 340°$ and they reach a maximum with a low $\gamma B_1/\sigma$ ratio and they disappear at large $\gamma B_1/\sigma$ ratios. This combination of requirements explains why the NQR SPEs have not been observed in previous NQR experiments. Echoes have been observed and predicted by theory in glycine hemihydrochloride and RDX. The theory and experiments allow us to characterize SPEs as temporally asymmetric with a fast initial rise. While the experimental confirmation of this theory utilized samples with a large EIB and a pow-

der sample, which contributes to inhomogeneous Rabi broadening, this theory should be applicable to other systems with inhomogeneous line broadening and inhomogeneous Rabi broadening whatever the cause.

Additionally, the theories for SPEs and DPEs are compared and we find that the SPE behaves like a DPE with no time between pulses and that the SPE $\sigma\text{Signal}_{\text{total}}$ can be greater than the DPE $\sigma\text{Signal}_{\text{total}}$ under certain conditions. This is shown using glycine hemihydrochloride and a pulse such that $\gamma B_1/\sigma = 1.03$. An analysis of the DPE, using this model, also provides additional insight into the experimentally observed increased delay of the DPE. The delay of the DPE ($\Delta\tau$) is the difference between our theoretical predictions and the predictions using an ideal delta-pulse. The theory predicts $\Delta\tau = 0.62 t_1$ at large values of $\gamma B_1/\sigma$ in a powder and is only 2% less at small values of $\gamma B_1/\sigma$ and this is confirmed by experiments. Therefore, using these techniques, pulse sequences for the detection of contraband over a large volume can be tuned for an optimum SPE or DPE signal.

Appendix. Fictitious spin-$\frac{1}{2}$ Operators

For spin-1 the eigenfunctions of I_z are $|+1>, |-1>$, and $|0>$. The eigenfunctions of H_Q in the principle axis frame of the electric field gradient are: $|+> = (|+1> + |-1>)/\sqrt{2}, |-> = (|+1> - |-1>)/\sqrt{2}$, and $|0> = |0>$, and have the corresponding eigenenergies: E_+, E_-, and E_0. The NQR transition frequencies are: $\omega_x = (E_+ - E_0)/\hbar, \omega_y = (E_0 - E_-)/\hbar$, and $\omega_z = (E_- - E_+)/\hbar$.

The fictitious spin-$\frac{1}{2}$ operators are:

$$I_{x1} = \tfrac{1}{2}I_x; \qquad I_{y1} = \tfrac{1}{2}I_y; \qquad I_{z1} = \tfrac{1}{2}I_z;$$
$$I_{x2} = \tfrac{1}{2}(I_yI_z + I_zI_y); \quad I_{y2} = \tfrac{1}{2}(I_xI_z + I_zI_x); \quad I_{z2} = \tfrac{1}{2}(I_xI_y + I_yI_x);$$
$$I_{x3} = \tfrac{1}{2}(I_z^2 - I_y^2); \qquad I_{y3} = \tfrac{1}{2}(I_x^2 - I_z^2); \qquad I_{z3} = \tfrac{1}{2}(I_y^2 - I_x^2);$$
$$I_{x4} = I_{y3} - I_{z3}; \qquad I_{y4} = I_{z3} - I_{x3}; \qquad I_{z4} = I_{x3} - I_{y3}.$$

and $I_\pm = (I_{x1} \pm iI_{x2})/2$.

These operators meet the condition $I_{x3} + I_{y3} + I_{z3} = 0$, and the power of these operators is in the commutation relationships. A few examples are

$$[I_{p,i}, I_{p,4}] = 0, \tag{10}$$
$$[I_{p,i}, I_{p,j}] = iI_{p,k}, \tag{11}$$

where i, j, k are cyclic and where $p \in (x, y, z)$.

References

[1] A.N. Garroway, M.L. Buess, J.B. Miller, B.H. Suits, A.D. Hibbs, G.A. Barrall, R. Matthews, L.J. Burnett, Remote sensing by nuclear quadrupole resonance, IEEE Trans. Geoscience and Rem. Sens. 39 (2001) 1108.
[2] B.H. Suits, A.N. Garroway, J.B. Miller, K.L. Sauer, ^{14}N magnetic resonance for materials detection in the field, Solid State Nucl. Magn. Reson. 24 (2003) 123.
[3] J.B. Miller, G.A. Barrall, Explosives detection with nuclear quadrupole resonance, American Scientist 93 (2005) 50.
[4] Y.E. Lee, Spin-1 nuclear quadrupole resonance theory with comparisons to nuclear magnetic resonance, Concepts Magn. Reson. 14 (2002) 155–171.
[5] A.L. Bloom, Nuclear induction in inhomogeneous fields, Physical Review 98 (1954) 1105.
[6] M. Stearns, Origin of the single pulse echo in Co, AIP Conf. Proc. 10 (1973) 1644.
[7] L.N. Shakhmuratova, D.K. Fowler, D.H. Chaplin, Fundamental mechanisms of single-pulse NMR echo formation, Phys. Rev. A 55 (1997) 2955.
[8] I. Kiliptari, V. Tsifrinovich, Single-pulse nuclear spin echo in magnets, Physical Review B 57 (1998) 11554.
[9] A. Akhalkatsi, G. Mamniashvili, S. Ben-Ezra, On mechanisms of single-pulse echo formation in multidomain magnetic material, Physics Letters A 291 (2001) 34.

[10] A. Akhalkatsi, M. Zviadadze, G. Mamniashvili, N. Sozashvili, A. Pogorelyi, O. Kuzmak, Multipulse analogs of signals of the single-pulse echo in multidomain magnetic material, The Physics of Metals and Metallography 94 (2004) 252.

[11] Y.M. Bunkov, B. Dumesh, M. Kurkin, Single-pulse echo in systems with dynamic frequency shift, JTEP Lett. 19 (1974) 132.

[12] R. Brewer, R. Showmaker, Optical free induction decay, Phys. Rev. A 6 (1972) 2001.

[13] A. Schenzle, N. Wong, R. Brewer, Oscillatory free-induction decay, Phys. Rev. A 21 (1980) 887.

[14] V. Kuzmin, I. Rutkovskii, A. Saiko, A. Tarasevich, G. Fedoruk, Free induction and echo during nonresonant excitation of inhomogeneously broadened NMR line, Soviet Physics JTEP 70 (1990) 493.

[15] A. Ponti, Single-pulse echo and the oscillatory free induction decay: the importance of rephasing, Molecular Physics 95 (1998) 943.

[16] R. Kaiser, The edge echo, J. Mag. Res. 42 (1981) 103.

[17] V. Chekmarev, V. Malyshev, Single-pulse echo in spin systems, Soviet Physics Solid State 30 (1988) 911.

[18] I. Rutkovskii, A. Tarasevich, G. Fedoruk, Single-pulse echo in spin systems, Soviet Physics Solid State 31 (1989) 713.

[19] E.L. Hahn, Spin echoes, Phys. Rev. B 80 (1950) 580.

[20] G. Fedoruk, Single-pulse echo and its secondary signals in two-level spin systems, Journal of Applied Spectroscopy 71 (2004) 339.

[21] S. Vega, A. Pines, Operator formalism for double quantum NMR, J. Chem. Phys. 66 (1977) 5624.

[22] R.S. Cantor, J.S. Waugh, Pulsed spin locking in pure nuclear quadrupole resonance, J. Chem. Phys. 73 (1980) 1054.

[23] C. Cohen-Tannoudji, B. Diu, F. Laloe, Quantum Mechanics, vol. 2, John Wiley and Sons, 1977.

[24] A. Abragam, Principles of Nuclear Magnetism, Clarendon Press, Oxford, 1961.

[25] A. Kentgens, Off-resonance nutation nuclear magnetic resonance spectroscopy of half-integer quadrupolar nuclei, Progress in Nuclear Magnetic Resonance Spectroscopy 32 (1998) 141.

[26] C.P. Slichter, Principles of Magnetic Resonance, third ed., Springer-Verlag, 1996.

[27] G. Bodenhausen, R. Freeman, D. Turner, Suppression of artifacts in Two-Dimensional J spectroscopy, J. Mag. Res. 27 (1977) 511.

[28] B. Bandyopadhyay, G. Furman, S.D. Goren, C. Korn, A. Shames, One pulse spin-locking in NQR, Z. Naturforsch 51a (1996) 357.